

3D, 9C seismic modeling and inversion of Weyburn Field data

Herurisa Rusmanugroho¹ and George A. McMechan²

ABSTRACT

Inversion of 3D, 9C wide azimuth vertical seismic profiling (VSP) data from the Weyburn Field for 21 independent elastic tensor elements was performed based on the Christoffel equation, using slowness and polarization vectors measured from field data. To check the ability of the resulting elastic tensor to account for the observed data, simulation of the 3C particle velocity seismograms was done using eighth-order, staggered-grid, finite-differencing with the elastic tensor as input. The inversion and forward modeling results were consistent with the anisotropic symmetry of the Weyburn Field being orthorhombic. It was dominated by a very strong, transverse isotropy with a vertical symmetry axis, superimposed with minor near-vertical fractures with azimuth $\sim 55^\circ$ from the inline direction. The predicted synthetic seismograms were very similar to the field VSP data. The examples defined and provided a validation of a complete workflow to recover an elastic tensor from 9C data. The number and values of the nonzero tensor elements identified the anisotropic symmetry present in the neighborhood of a 3C borehole geophone. Computation of parameter correlation matrices allowed evaluation of solution quality through relative parameter independence.

INTRODUCTION

Background and context

Three-component (3C) geophones in vertical seismic profiles provide a unique opportunity to sample the material properties in the neighborhood of the borehole. This is a consequence of the inherent potential for sampling incident waves in wide azimuth

and polar angle apertures (Rusmanugroho and McMechan, 2012). When the medium in which a 3C geophone is located is anisotropic, the local anisotropic elastic moduli can be estimated from the quasi-P (qP), the faster quasi-S₁ (qS₁), and slower quasi-S₂ (qS₂) phase slownesses and polarizations (de Parscau and Nicoletis, 1990; Zheng and Pšenčík, 2002; Dewangan and Grechka, 2003).

The feasibility of extracting elastic moduli from phase slownesses and polarizations is analyzed by Norris (1989), Jech (1991), Ditri (1994), and Dewangan and Grechka (2003). Theoretically, as few as six wave propagation directions are sufficient to extract all 21 elastic moduli when all of the qP, qS₁, and qS₂ waves are present (Norris, 1989), if these six directions are optimal.

Inversion for the 21 elastic moduli is based on the Christoffel equation (see the Inversion subsection in the “Methodology” section). The Christoffel equation relates the density-normalized elastic moduli of the medium (the output of the inversion) to the qP, qS₁, and qS₂ wave slownesses and polarizations (the inputs to the inversion). The Christoffel equation itself does not specify which quantities are input and which are output, so a variety of combinations can be input and the others solved for. In the first field data inversion below, approximate horizontal slownesses are estimated from time difference between direct sources from surface waves and used as part of the input data; in the second, the horizontal slownesses of both the qP and qS waves are treated as unknowns. The latter is more realistic as horizontal slownesses cannot be measured in a borehole.

Previous work at the Weyburn Field

The Weyburn Field is located in the Williston Basin in southeastern Saskatchewan in Canada (Figure 1). The Weyburn Field produces oil from the Midale carbonate reservoir (in Figure 2), which contains marly and vuggy units (e.g., Bunge, 2001; Davis et al., 2002). The marly unit is characterized by high porosity (26%) and low permeability (10 md), and the underlying vuggy unit is characterized by low porosity (11%) and high permeability (15 md). The seismic character of the overburden above the

Manuscript received by the Editor 11 October 2011; revised manuscript received 31 January 2012; published online 18 June 2012.

¹Formerly The University of Texas at Dallas, Center for Lithospheric Studies, Richardson, Texas, USA; presently WesternGeco/Schlumberger, Houston, Texas, USA. E-mail: HRusmanugroho@slb.com.

²University of Texas at Dallas, Center for Lithospheric Studies, Richardson, Texas, USA. E-mail: mcmec@utdallas.edu.

© 2012 Society of Exploration Geophysicists. All rights reserved.

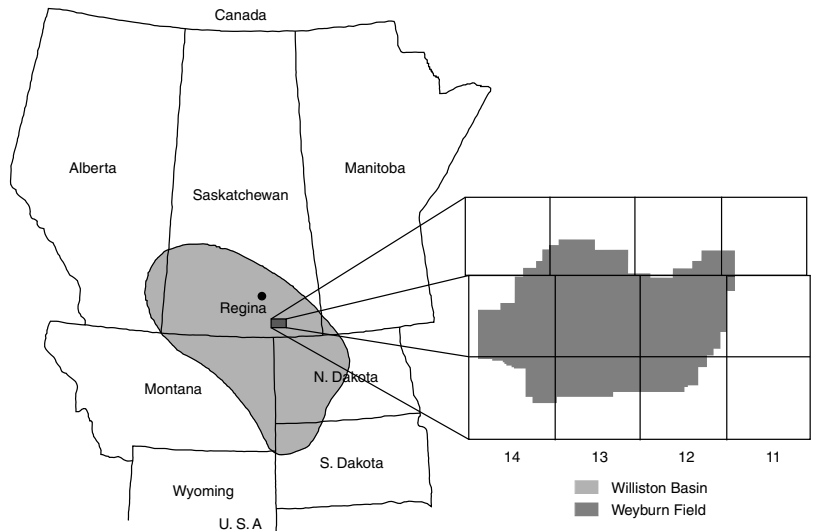


Figure 1. Location map of the Weyburn Field in the Williston basin distributed over Townships 5, 6, and 7, and Ranges 11, 12, 13, and 14 (adapted from Wegelin, 1984).

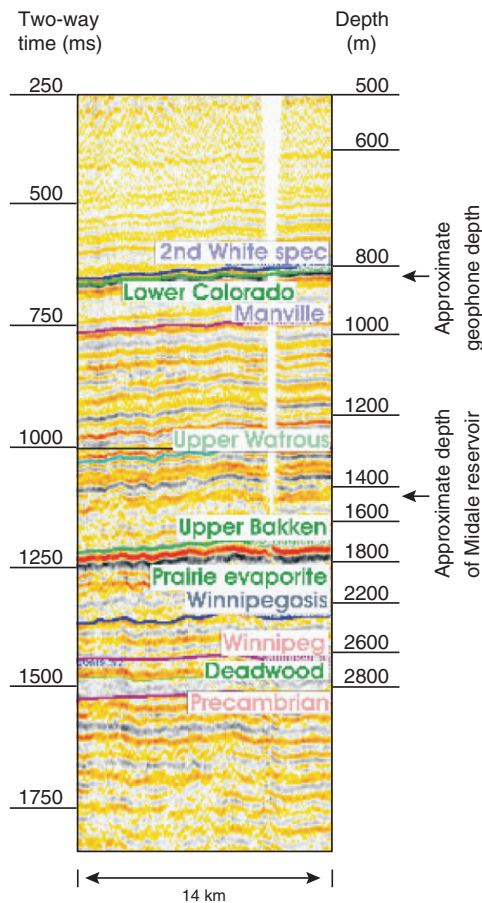


Figure 2. Stratigraphic markers of the Weyburn region superimposed on a representative seismic section (modified from White et al., 2004). The seismic line does not go through the well; the depths at this location are approximately 80 m shallower than where the VSP data were acquired, but the seismic character of the lithology (especially the homogeneity of the shallow overburden) is clearly seen.

VSP array used to record the data used in this paper is quite homogeneous (Figure 2); the lithology is primarily shales with a few sand layers (Wilson and Monea, 2004).

Fractures are an important reservoir feature; connected, high-density cracks can increase porosity and permeability. Laboratory measurements by Jones and Wang (1981) on cores from the Williston basin in North Dakota show that the Cretaceous shales possess VTI symmetry. Bunge (2001) identifies two healed, and three open, fracture sets in the cores and logs. Davis et al. (2002) note that CO₂ flooding in the Weyburn Field, which is controlled by faulted and fractured zones, has improved the oil production by at least 15% since October 2000. Thus, characterization of the fractures and the resulting anisotropy is of practical, economic significance.

Reasnor (2001) combines well logs, cores, and theoretical models to generate rock-physics models of the marly and vuggy reservoir units, and concludes that the cracks have large effects on

the slow S-wave compared to those on the P- and fast S-waves. Jenner (2001) shows azimuthal anisotropic velocity variations which reach ~6% above and in the reservoir from 3D compressional wave data. Adam (2003) concludes that there is no significant dip of the stratigraphic layers in the Weyburn Field.

Nine-component seismic data provide the best, most complete, technology possible for reservoir characterization. Davis et al. (2002) note that the S-waves from the horizontal sources are more sensitive to the vuggy unit and the P-waves from the vertical sources are more sensitive to the overlying marly unit. Rusmanugroho and McMechan (2010) show that the P-wave generated from the vertical force source, and the S-wave generated from the horizontal force source that is parallel to the *x*-axis, are the most diagnostic for cracks parallel to the *y*-axis. Rusmanugroho and McMechan (2012) also demonstrate that 9C wide azimuth VSP data can resolve the complete elastic stiffness tensor for the most complicated anisotropic symmetry (triclinic), provided that the polar angle and azimuth apertures are sufficiently large, and analyze the sensitivity of the estimated elastic moduli to data completeness of wave type, measurement type, and illumination apertures at a receiver in multicomponent VSP data. That sets the stage for the present paper, which focuses on complete analysis of a high quality VSP data set, inference of symmetry from the inverted tensor, and use of parameter correlation matrices to evaluate the solution.

The goal in this paper is not to develop new technology, but to use the current state-of-the-art applied to what is perhaps the best, most complete, data set of its kind that is available today. We invert 3D, 9C wide azimuth VSP data from the Weyburn Field to estimate the 21 independent elastic tensor elements from the measured slowness and polarization vectors. This is the application of the inversion algorithm previously described by Dewangan and Grechka (2003) and Rusmanugroho and McMechan (2012) to the Weyburn Field data. The objective function is evaluated only for the slowness and polarization data.

Finally, to close the loop, we do forward modeling using the inverted elastic tensor elements and compare the predicted synthetic seismograms with the observed Weyburn Field seismograms. The

predicted synthetic seismograms are quite similar to those in the field VSP data from the Weyburn Field.

3D, 9C WIDE AZIMUTH VSP DATA

Figure 3 shows the 3D, 9C VSP survey geometry at the Weyburn Field. Data acquisition was conducted by the Reservoir Characterization Project at the Colorado School of Mines in 2001. Each black dot is one of 1253 3C vibroseis sources. The average source spacing is 40 m in the crossline and inline directions. The red and blue triangles define the lines X and Y, which contain the sources for the representative VSP data shown in the later figures. The lines X and Y contain 64 and 28 source points, respectively. The green circle is the borehole location.

The 3D, 9C wide azimuth VSP data are recorded by four 3C geophones located from 887.1 to 932.1 m depth with a 15 m interval. The details of the acquisition are described by Adam (2003) and Bellefleur et al. (2003, 2004). The data apertures of the Weyburn Field data cover 0° – 360° for azimuth and 0.04° – 68° for polar angle (Figure 3). These apertures are sufficient for inversion of all 21 elastic tensor elements (Rusmanugroho and McMechan, 2012).

METHODOLOGY

The data processing contains three main parts. First, preprocessing involves virtual rotation of the geophones into the anisotropic axes and calculations of the slownesses and polarizations. Second, the inversion involves fitting the estimated slownesses and polarizations to estimate the 21 elastic tensor elements via the Christoffel equation. The inversions are done in two ways. In the first approach, the horizontal slownesses are approximated by differencing the times of the direct waves between pairs of sources (at the surface); these are input as data along with the qP, qS₁, and qS₂ polarizations and the vertical slowness (measured vertically in the borehole), to estimate the 21 elastic moduli. In the second approach, the horizontal slownesses are estimated along with the 21 elastic moduli. Dewangan and Grechka (2003) refer to these two situations as their scenarios one and three, respectively. The third and final step is to input the estimated elastic moduli into 3D elastic finite differencing, to generate synthetic 3D, 9C data to compare with the input data to evaluate the quality of the solution. In this section, we now describe each of these steps.

Data preprocessing

The preprocessing data of the field plays a key role in the inversion. The quality of the data determines the quality of the inversion results. A 10–20–60–70 Hz bandpass filter is applied. Three-component gaining is applied using ProMAX (by the Geological Survey of Canada).

Assuming the hole is vertical and the anisotropy is weak, three rotations of the horizontal geophone data are performed. The first involves an estimation of the unknown orientations of the horizontal geophones. This is done by rotating the horizontal geophones so that the direct P-wave amplitude is maximized in one component and minimized in the other; these are the radial and transverse components, respectively

(DiSiena et al., 1984). For each source, this estimates the P-wave rotation angle relative to the original unknown geophone orientation. Then, the radial and transverse components are projected into the inline and crossline directions, by assuming that the P-wave polarization and propagation directions are the same (Adam, 2003; Dewangan and Grechka, 2003; Zhang, 2011). Zhang and McMechan (2011) quantify the errors in this assumption and show that they are $<5\%$ for most sedimentary rocks ($\epsilon, \delta < 0.2$); Davis et al. (2002) show that this effect is smaller for S-waves than for P-waves.

The third step is to separate the qS-waves into qS₁ and qS₂ by maximizing and minimizing the polarizations of the direct qS-waves; the diagonal amplitudes (XX and YY) are maximized and the off-diagonal amplitudes (XY and YX) are minimized (Figure 4) (Alford, 1986). The resulting rotation angle is then also applied to the rest of the nine components (although, for example, there is no change to ZZ). Note that only relative amplitudes are involved in the polarization computation. The data processing flow is nicely summarized by Michaud (2001). The polarization vector components are now parallel and perpendicular to the dominant anisotropic axes. The vertical component of slowness is calculated from traveltimes differences. These polarization and slowness components are input to the inversion.

If the material between the surface and the borehole geophone is homogeneous, horizontal phase slownesses for each of qP, qS₁, and qS₂ can be approximated by taking the first derivative of traveltimes with respect to the source (surface) positions (e.g., Gaiser, 1990). Before calculating the horizontal slownesses, the sparse and non-uniform horizontal source locations are resampled with a 10-m increment. Phase slownesses measured from the resampled data are interpolated to give the values at the actual source locations. There is no significant lateral heterogeneity associated with velocity variations or stratigraphic dip at this site (Jenner, 2001; Adam, 2003). To increase the stability of the estimated horizontal phase

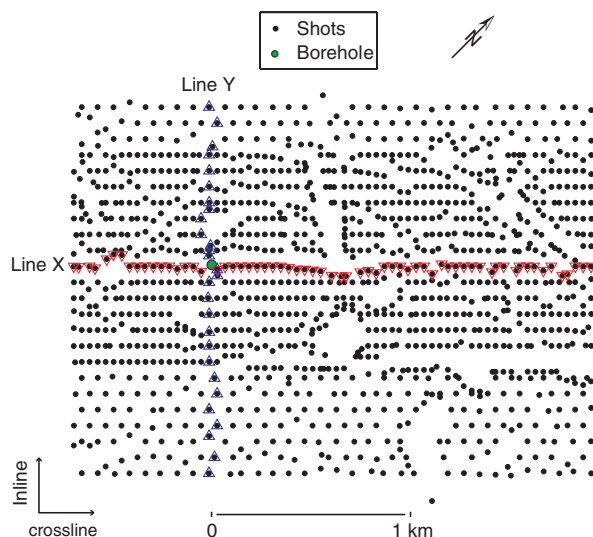


Figure 3. 3D, 9C wide azimuth VSP source geometry (black dots). The VSP borehole (green circle) is located at (0,0, 0.0) km. The red and blue triangles show source positions for the lines X and Y which are parallel and perpendicular to the crossline, respectively. Four 3C geophones are located in the borehole from 887.1 to 932.1 m depth.

slownesses, smoothing is applied over a moving 5×5 point (40×40 m) rectangle. To calculate vertical phase slowness at the receiver located at 902.1 m depth, the time derivative with depth (dt/dz) is calculated by differencing the direct wave times across receivers at 887.1 and 917.1 m centered at 902.1 m depth.

Inversion

The two inversions presented below correspond to scenarios one and three of Dewangan and Grechka (2003). Scenario one includes the horizontal slowness components, estimated at the surface, as part of the input data, and solves only for the elastic moduli; scenario three solves for the horizontal slowness components along with the (density-normalized) elastic moduli. In scenario one, the inversion is linear and stable and can be solved directly from the Christoffel equation; in scenario three, the inversion is underdetermined, nonlinear, and iterative. The presence of even a small amount of noise makes scenario one also nonlinear.

We choose to always solve for 21 moduli and let the number and distribution of nonzero components reveal the actual anisotropy

symmetry. It is also possible, if a priori information is available on the appropriate symmetry, to correspondingly reduce the number of moduli to be solved for. Another possible strategy is to perform a series of inversions, each assuming a different possible anisotropic symmetry, and then to select the most likely one, on the basis of it being to adequately fit the main features in the data with the least number of moduli. (These are not done here; they are left for future investigation). The starting model for the inversions below is based on measurements of the host rock parameters (equation A-1 in Appendix A).

The solution of the inverse problem of estimating 21 independent elastic moduli from polarization and slowness vectors for qP , qS_1 , and qS_2 waves is based on the Christoffel equation. Following Dewangan and Grechka (2003), the Christoffel misfit (F) can be written

$$F_i^{(Q)} \equiv G_{ik} A_k^{(Q)} - A_i^{(Q)}, \tag{1}$$

where A is the unit normalized polarization vector, and G is the symmetric Christoffel matrix with

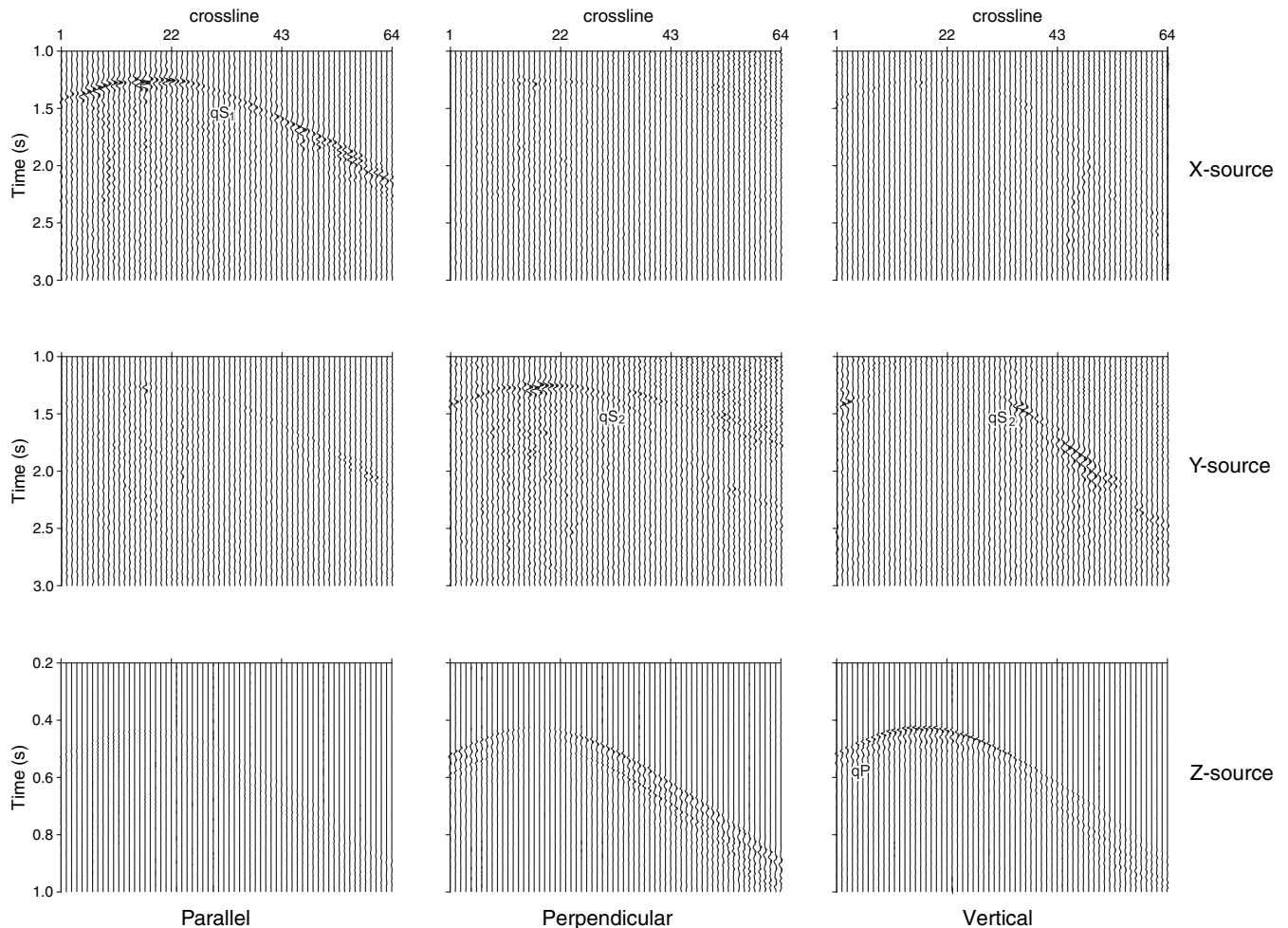


Figure 4. These panels show the representative processed 3D, 9C VSP wide azimuth data, along the line X (through the borehole recorded on the geophone at 902.1 m depth, parallel to the crossline) in Figure 3. For visibility, the Z-source components are plotted with an amplitude scale factor that is two times larger than those of the X- and Y-source components. Some first arrivals for the fast and slow S-waves (qS_1 and qS_2), and for the P-wave (qP), are labeled.

$$G_{ik} = c_{ijkl}P_jP_l, \quad (2)$$

for

$$Q = qP, qS_1, qS_2; \quad \text{and} \quad i, j, k, l = 1, 2, 3.$$

Here, \mathbf{c} is the density-normalized elastic tensor, and \mathbf{p} is the slowness vector. For any chosen propagation direction, three slowness vectors and three polarizations will exist (i.e., one for each Q).

The inverse problem is performed using the iterative Levenberg-Marquardt algorithm (Moré, 1977). See Rusmanugroho and McMechan (2012) for examples. The model parameter vector at iteration $n + 1$ is

$$\mathbf{m}_{n+1} = \mathbf{m}_n + [\mathbf{J}_n^T \mathbf{J}_n + \epsilon^2 \mathbf{I}]^{-1} \mathbf{J}_n^T \mathbf{K}_n (\mathbf{d}^{\text{obs}} - \mathbf{d}_n^{\text{cal}}). \quad (3)$$

The model vector \mathbf{m} contains the elastic tensor elements to be solved for. The data vector \mathbf{d} contains the qP , qS_1 , and qS_2 wave polarizations and slownesses. \mathbf{J} is a Jacobian matrix containing the first derivatives of the Christoffel equation with respect to each of the model parameters, \mathbf{K} is a diagonal matrix containing the derivative of the Christoffel equation with respect to the data vector and \mathbf{I} is an identity matrix. The term ϵ is a damping factor. Superscripts -1 and T define inverse and transpose; superscripts “obs” and “cal” refer to the observed and calculated data, respectively.

The solution is obtained by minimizing the objective function of the root mean square misfit

$$\Phi_{\text{rms}} = \sqrt{\frac{1}{N} \sum_{i=1}^N \mathbf{F}^2}, \quad (4)$$

where \mathbf{F} is the Christoffel equation residual given by equation 1 and N is the number of sources (e.g., Dewangan and Grechka, 2003; Kochetov and Slawinski, 2009).

Forward modeling

To close the loop, forward modeling is performed, based on the velocity-stress relation of the elastodynamic equations for general anisotropy (Tessmer, 1995) implemented by eighth-order, staggered-grid, finite-differencing (Ramos-Martínez et al., 2000).

The inputs to the modeling are the recording geometry (Figure 3), and the elastic tensor estimates that are produced as the output of the inversion (equation A-3 in Appendix A). The latter is strictly applicable only to the neighborhood (within a couple wavelengths [Nistala and McMechan, 2005]) of the 3C geophone, but is also appropriate if the earth is homogeneous above the geophone (Gaiser, 1990); this assumption is tested for the Weyburn VSP data below. The outputs of the modeling are 3C particle velocity seismograms that can be compared to the field VSP data.

For the modeling, the source time function is a Gaussian wavelet of 26 Hz, the time sample

increment is 0.0008 s, and the total recording time 4 s. The grid increment is 10 m and the model grid size is $(x, y, z) = (3000, 2500, 1500)$ m.

INVERSION RESULTS

Figure 4 shows representative processed 3D, 9C wide azimuth field VSP data, along the line X (through the borehole recorded on the geophone at 902.1 m depth, parallel to the crossline axis) in Figure 3. The top, center, and bottom rows of panels in Figure 4 contain the data generated from the X-, Y-, and Z-oriented vibroseis sources; the left, center, and right columns contain the components of the data that are rotated to be parallel, perpendicular, and vertical to the fast (qS_1) and slow (qS_2) polarizations.

In Figure 4, the data generated by the three (X, Y, Z) component sources and recorded on the three (X, Y, Z) component receivers are rotated to maximize the separation between qS_1 and qS_2 (as described by Alford [1986]). Now, these components are oriented parallel and perpendicular to the anisotropy orientation. The amplitudes in the (X-source, perpendicular) and (Y-source, parallel) components are nearly zero, indicating that the Alford rotation worked well. The qS_1 and qS_2 are seen at nearly the same traveltimes in the

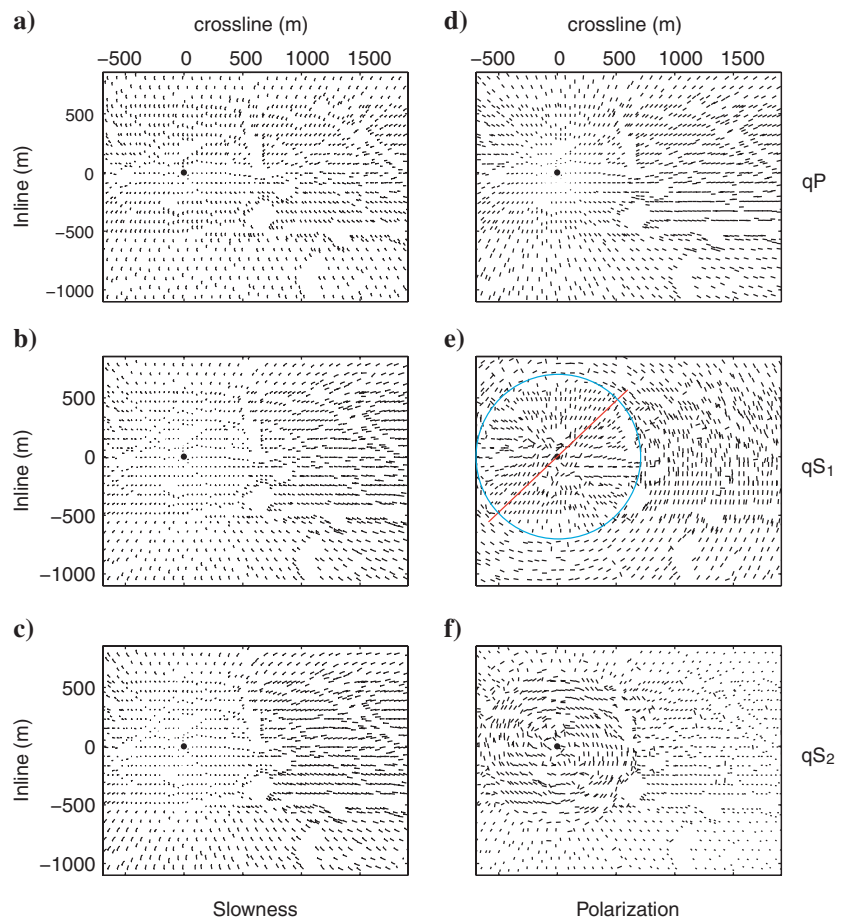


Figure 5. Horizontally projected slowness and polarization vectors, are in the left and right panels, respectively, for qP (a and d), for qS_1 (b and e), and for qS_2 (c and f), measured from the Weyburn Field data. In (e), the blue circle is the singularity in qS where the radially and transversely polarized wavefronts pass through each other, and the red line is the estimated strike of the vertical fractures.

near offsets, for which the sources are close to the borehole. The qS_1 and qS_2 are well separated in time when the sources are located in the mid-to-far offsets. The approximation of computing the horizontal slowness at the surface, between sources, is more accurate at near offsets, and gets progressively less accurate as offset increases.

The left and right panels of Figure 5 show the slowness and polarization vectors projected to the horizontal plane, for qP (Figure 5a and 5d), for qS_1 (Figure 5b and 5e), and for qS_2 (c and f), measured from the Weyburn Field data. The horizontal slownesses are approximated between sources along the surface, not at the geophone. The slownesses of qP , qS_1 , and qS_2 (Figure 5a, 5b, and 5c) are all approximately radial, and all three look similar. Near the borehole, the slownesses are dominated by the vertical component, so the horizontal slowness components are close to zero. As the polar angles become wider, the horizontal slowness components become larger and the vertical components decrease.

As expected in a VTI-dominated medium, qP polarizations recorded from sources near the borehole are near vertical (Figure 5d). As the polar angles become wider, the qP polarizations become more horizontal. The horizontal projections of the qP polarizations are approximately radially oriented (Figure 5d). For the fast S-wave (qS_1) (Figure 5e), the horizontal projections of the polarizations near to the borehole are dominantly radial; for sources further away from the borehole, the polarizations become transverse. For the slow S-wave (qS_2) (Figure 5f), the polarizations are orthogonal to those of qS_1 , as predicted by the theory (e.g., Carcione, 2007). The change in polarization direction in the qS_1 and qS_2 plots is a consequence of a singularity in the corresponding propagation direction. The transversely polarized S-wavefront crosses the radially polarized S-wavefront to change from being the slowest to being the fastest, and vice versa (see Dellinger, 1991).

Figure 6a and 6b shows the initial and final inverted tensor elements for the full Weyburn Field data set with horizontal slowness components (in the left column), and without (in the right column), and with polarizations as inputs. Figure 6a and 6d are the output of the inversions, Figure 6b and 6e are the corresponding rms residuals of the Christoffel equation as a function of iteration number (equations 1 and 4), and Figure 6c and 6f are the model parameter correlations, respectively.

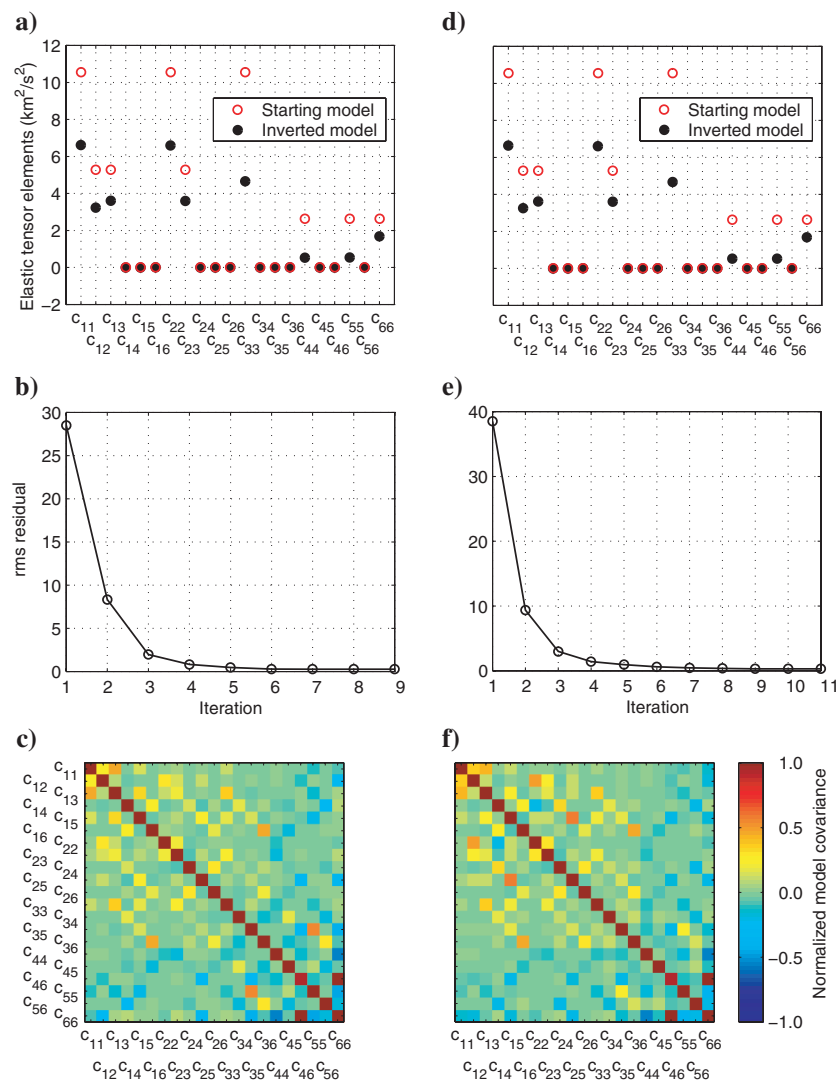


Figure 6. Inversion results for the Weyburn Field data with horizontal slowness components (in the left column), and without (in the right column). (a and d) are the output of the inversions, (b and e) are the rms residuals as a function of iteration number, and (c and f) are the normalized model covariance matrices, respectively.

The inversions converged in nine iterations with the rms residual of 0.274 (Figure 6b), and in eleven iterations with the rms residual of 0.281 (Figure 6e). The residuals are unitless (see equations 1 and 4). The solutions are obtained by minimizing the rms misfit Christoffel equation (equations 1 and 4).

In Figure 6c and 6f, the normalized model covariance (the correlation) values (Menke, 1989) on the diagonal indicate strong positive correlation of all the elements with themselves and hence, their independence of each other. The green and blue (near zero) values in the off-diagonal positions indicate weak relationships of between the element pairs. There are some element pairs indicating significant coupling (e.g., c_{66} and c_{46}); both of these have horizontally polarized shear strains which, for c_{66} is produced by a horizontal shear stress, and for c_{46} is produced by a vertical shear stress. Overall, the solution is very complete using the available (wide) polar angle (0.04° – 68°) and azimuth (0° – 360°) apertures. The two solutions are nearly the same, showing that the horizontal slownesses are not needed; they are redundant. This is consistent with the conclusion of Rusmanugroho and McMechan (2012), and previously illustrated by Dewangan and Grechka (2003).

The inversion results (equations A-2 and A-3 in Appendix A) show that there are large values on the diagonal of the tensor (c_{11} , c_{22} , c_{33} , c_{44} , c_{55} , and c_{66}) and on some of the off-diagonal (c_{12} , c_{13} , and c_{23}) components. The horizontal moduli pairs (c_{11} and c_{22} , and c_{44} , c_{55}) are similar, but not identical. This is consistent with the existence of small, azimuthally dependent cracks. Crack rotations generate other nonzero, and even negative, off-diagonal values (e.g., c_{15} , c_{25} , and c_{35} in A-2 and A-3) produced by the signs of the sines and cosines in the rotation transformation matrix (Helbig, 1994). Small negative values may also be produced by fitting noise for tensor values that are inherently small.

Crampin (1991) notes that the interactions of VTI and HTI contribute to form an orthorhombic medium that contains nine independent coefficients. Figure 6a and 6d show nine nonzero elements (to two decimal places), which is consistent with the conclusion of Adam (2003) that the medium is probably orthorhombic. The VTI and nonvertical cracks together can also create a monoclinic medium which contains 13 independent coefficients (Winterstein, 1990), but this is not consistent with the results in Figure 6, so the medium is not monoclinic.

Figure 7 shows horizontally projected slowness and polarization vectors for the elastic tensor solution with horizontal slownesses (in the left and right panels, respectively), for qP (Figure 7a and 7d), for qS₁ (Figure 7b and 7e), and for qS₂ (Figure 7c and 7f) calculated by the Christoffel equation. Both observed and calculated data (Figures 5 and 7) look similar, showing that the inversion works well. The blue (approximately circular) singularity is the boundary between the qSV- and SH-waves. The nearly circular shape affirms that the polarization is nearly VTI. If a stronger HTI was present, the singularity between the two qS polarizations would be distorted (e.g., Tessmer, 1995), with magnitude depending on the crack density, and with symmetry axes following the orientation of the cracks (e.g., Crampin, 1991). The red line in Figure 7e shows the estimated strike of the cracks, based on the relative amplitudes of the XY- and YX-components; this is about 55° to the inline direction, calculated using the Alford rotation.

Figure 8 shows horizontally projected slowness and polarization vectors (in the left and right panels, respectively), for the elastic tensor solution without horizontal slownesses in the input data, for qP (Figure 8a and 8d), for qS₁ (Figure 8b and 8e), and for qS₂ (Figure 8c and 8f) calculated, from the inverted moduli, by the Christoffel equation. Both observed and calculated data (in Figures 5 and 8, respectively) look similar, suggesting that the solution (Figure 8) accounts for most of the salient features in the data (Figure 5); the observed slownesses and polarizations are well reproduced by those in the synthetic seismograms calculated for the elastic moduli extracted from the field data. Additionally, the corresponding predicted polarizations and slownesses (Figures 7 and 8) are visually

indistinguishable, indicating that the horizontal slownesses are redundant (a numerical verification of the theoretical assertion of Dewangan and Grechka [2003] regarding their scenarios one and three). As seen by Rusmanugroho and McMechan (2012), omitting horizontal slownesses from the input data results in a slightly slower convergence rate (see Figures 6b and 6e), but does not significantly change the solution; the slower convergence is attributed to the lesser amount of input data.

FORWARD MODELING

To independently test the consistency of the inverted elastic tensor with the field data, we now simulate 9C data for the estimated tensor by finite-difference modeling. The modeling results are compared with the corresponding recorded 9C data; the main features of the field data are reproduced.

The modeling algorithm is a particle velocity-stress formulation of the elastodynamic equations (Tessmer, 1995) implemented by eighth-order, staggered-grid, finite differencing (Ramos-Martínez et al., 2000). The size of the model is $(x, y, z) = (301, 251, 151)$ grid points with 10-meter spacing (3000 × 2500 × 1500) m. The source wavelet is Gaussian, with a dominant frequency of

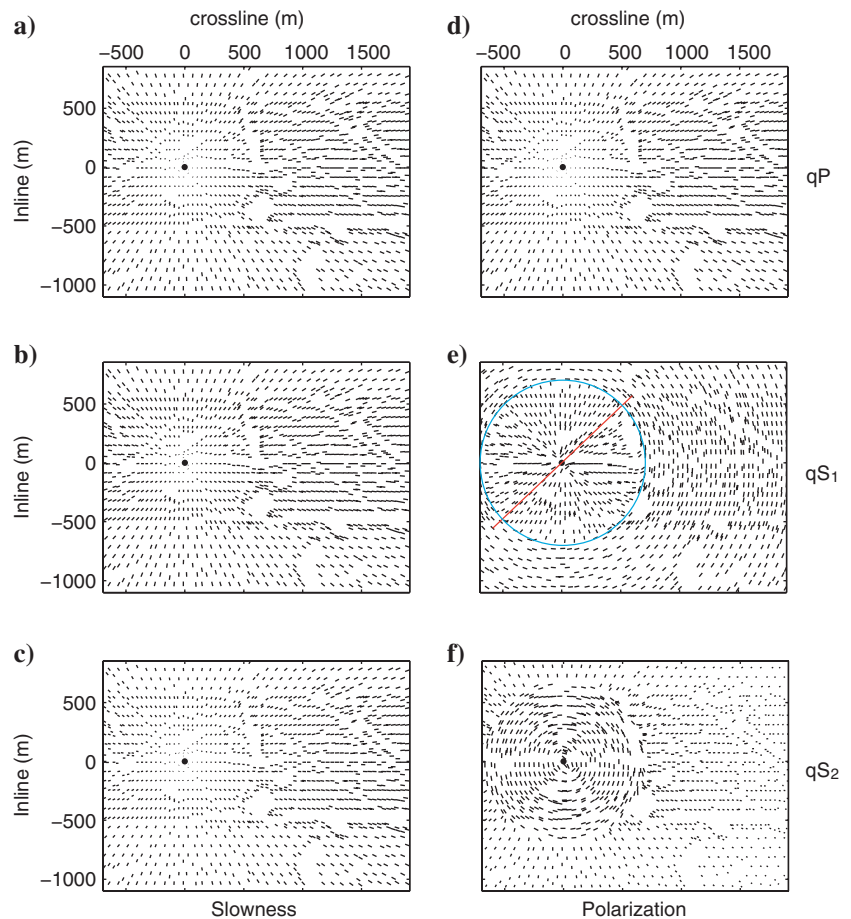


Figure 7. Horizontally projected slowness and polarization vectors are in the left and right panels, respectively, for qP (a and d), for qS₁ (b and e), and for qS₂ (c and f) calculated by the Christoffel equation from the elastic tensor elements obtained by the inversion with the horizontal slownesses in the data. The red line and blue circle (in e) show the strike of the small cracks oriented about 55° to the inline direction and the singularity of the qSV- and SH-waves, respectively.

26 Hz. For creating the synthetic test data, all six grid edges are absorbing, using Cerjan et al.'s (1985) tapering algorithm with tapering zone widths at the top, bottom, and vertical sides of 60, 20, and 40 grid points. The total recording time is 4.0 s with a time-sample increment of 0.0008 s. The 3C VSP receiver is located at $(x, y, z) = (0.0, 0.0, 902.1)$ m and the 3C orthogonal sources are distributed over the top of the model following the Weyburn survey geometry (in Figure 3). Because the evidence suggests that the material above the geophone is relatively homogeneous (see the subsection "Previous work at the Weyburn Field"), we invoke reciprocity to synthesize the data by placing a single 3C source at the actual receiver location and recording at the actual source locations (Rusmanugroho and McMechan, 2012). Because of the different conditions at the free surface and buried geophone, the amplitudes will be off by a factor of two (Sun and McMechan, 2008), but slowness and polarization will not be affected.

Modeling data along line X

Figure 9 shows a comparison between the nine Cartesian component synthetic seismograms created using the inverted elastic tensor elements, and the corresponding the 9C field seismograms from the Weyburn Field, for the line X marked in Figure 3. The X- and Y-source components, and the X- and Y-receiver components are oriented parallel to the crossline and inline axes, respectively (Figure 3).

The qP- and the two qS-waves show nearly the same traveltimes in the synthetic and the field data. In the field data, the amplitudes in the XY- and XZ-components are weak, and in the XX-component are strong; similarly, in the synthetic data. In the field data, amplitudes decrease suddenly in the YY-component; similarly, in the synthetic data.

There are weak amplitudes in the YZ-component of the field data in the near and far offsets, and large in the intermediate offsets; amplitudes are similar in the synthetic data. Close to the borehole, the amplitudes are almost zero in the ZY-components, and are correspondingly strong in the ZZ-component; amplitudes are similar in the synthetic data. The models for the synthetic and field data are homogeneous versus heterogeneous, respectively. In the field data, some reflection or multipathing events exist (e.g., in the field ZY-component) that are not modeled in the synthetic data.

In the modeled data in the YY- and YZ-components, a triplicated qS is seen, which is theoretically expected in strong VTI media (as described by Dellinger, 1991). The qS triplication is not as clearly defined in the field data, but the related amplitude focusing is visible.

In the field data, the XY- and YX-components contain small amplitudes indicating that the medium is not pure VTI. These amplitudes are consistent with the presence of cracks of small crack density, which produces an orthorhombic velocity with nonzero off-diagonal amplitudes. Similar small amplitudes are also seen in the synthetic data. By comparing carefully, the amplitudes in the YX

are relatively larger than those in the XY-components in both the field and synthetic data. Because the horizontal S-wave polarization will be parallel and perpendicular to the vertical fractures, the fracture orientation can be determined from the relative amplitudes of the YX- and XY-amplitude-vector components; on this basis, the cracks are oriented at an angle a bit greater than 45° from the inline direction.

Modeling data along line Y

Figure 10 shows a comparison between the nine Cartesian component synthetic seismograms created using the inverted elastic tensor elements, and the corresponding 9C field seismograms from the Weyburn Field, for the line Y marked in Figure 3. The spacing of sources along line Y is wider than along line X, so, these traces are more widely separated.

The qP and the two qS events in the synthetic and field data show nearly the same traveltimes indicating the inversion worked successfully. Similarly to the previous plots, we see the (low, but non-zero) amplitude effects of cracks in the XY- and YX-components. By comparing carefully, the amplitudes in the YX-component are slightly larger than those in the XY-component, in both the synthetic and the field data. Again, the cracks seem (qualitatively) to be oriented at an angle a bit greater than 45° to the inline axis (from the relative amplitudes), which is consistent with the

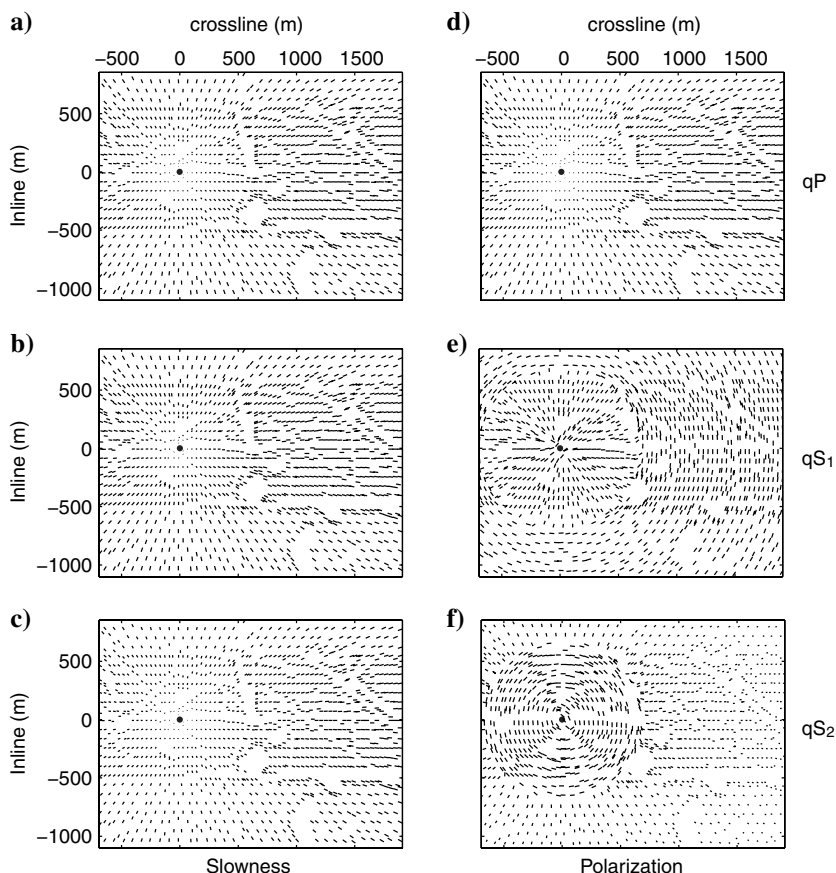


Figure 8. Horizontally projected slowness and polarization vectors, are in the left and right panels, respectively, for qP (a and d), for qS₁ (b and e), and for qS₂ (c and f) calculated by the Christoffel equation from the inverted elastic tensor elements without horizontal slownesses in the data. Compare with the measured data in Figure 5.

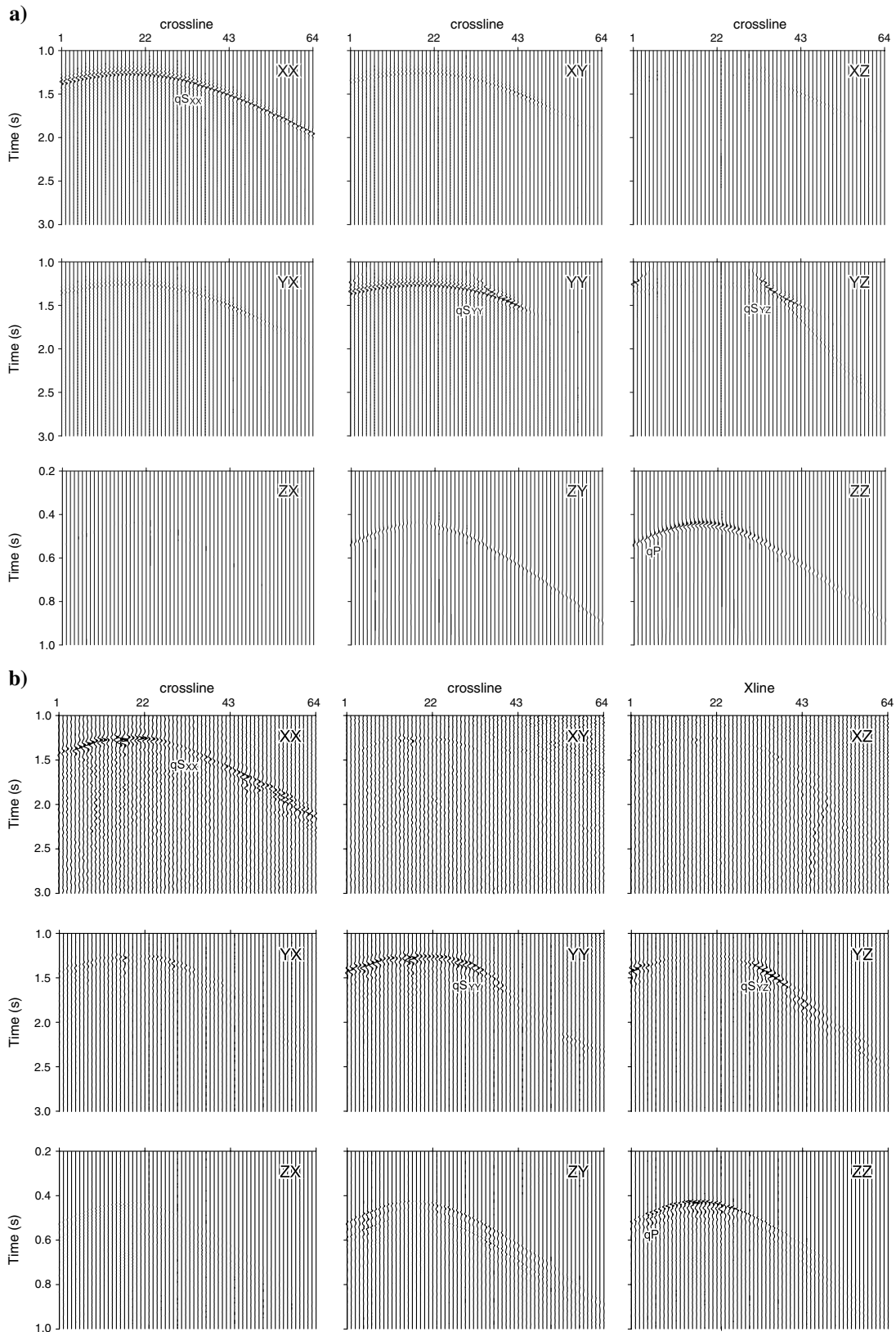


Figure 9. Representative 3D, 9C (a) synthetic Cartesian component seismograms created using the inverted elastic tensor elements without horizontal slownesses, and (b) the corresponding field seismograms from the Weyburn Field, along the line X (through the geophone 902.1 m, parallel to the crossline direction) in Figure 3. For clarity, the Z-source components are plotted with an amplitude scale that is a factor of two times larger than those of the X- and Y-source components in both the field and synthetic data.

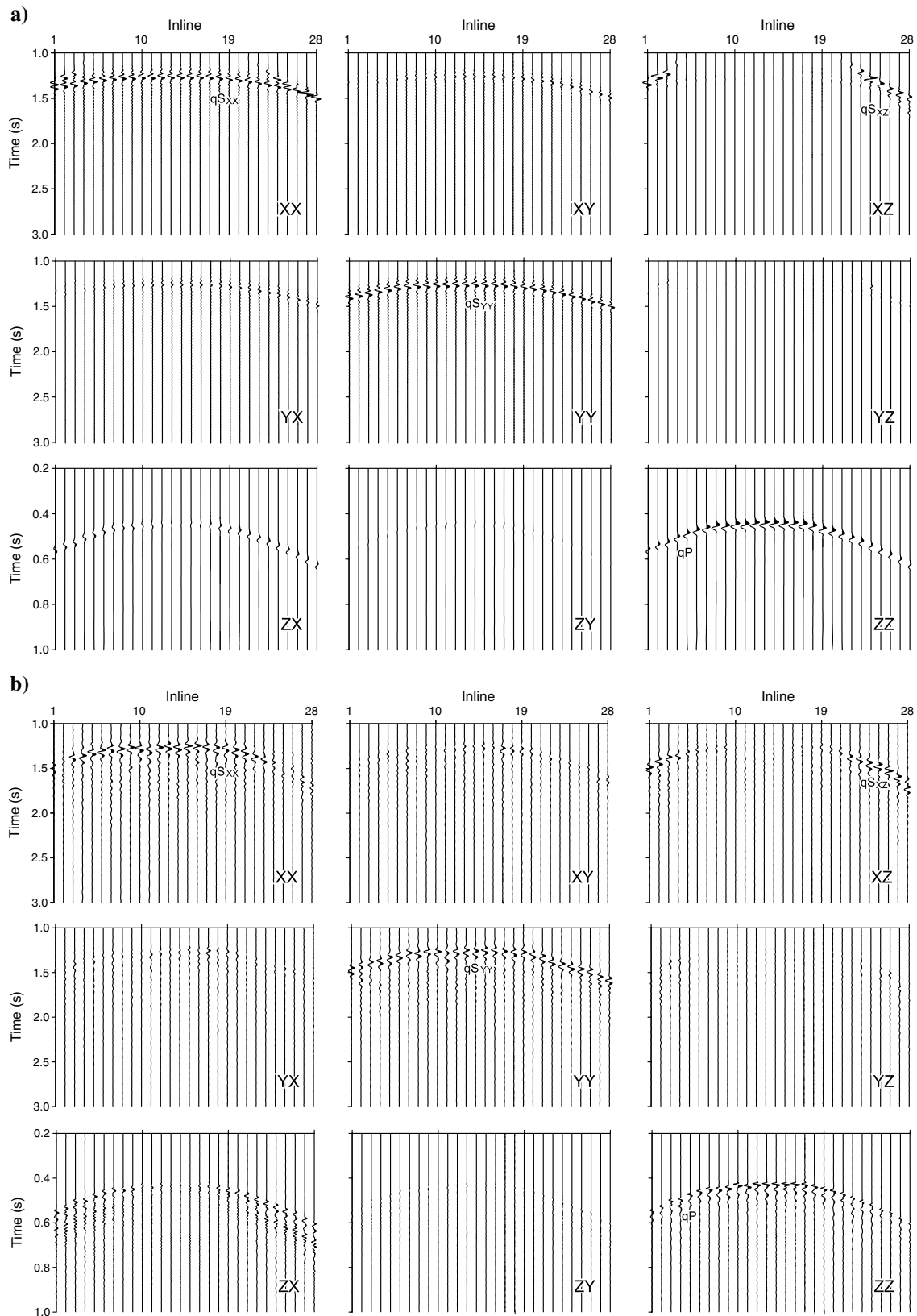


Figure 10. Representative unrotated 3D, 9C (a) synthetic Cartesian component seismograms created using the inverted elastic tensor elements without horizontal slownesses, and (b) the corresponding field seismograms from the Weyburn Field, along the line Y (through the geophone at 902.1 m, perpendicular to the crossline direction) in Figure 3. For clarity, the Z-source components are plotted with an amplitude scale that is a factor of two times larger than those of the X- and Y-source components in both the field and synthetic data.

observations in Figure 9. Quantitatively, the crack orientation angle is $\sim 55^\circ$ from the Alford rotation. In the ZX-component of the field data, the later arrivals may be deeper reflections, or converted waves, or internal multiples.

Because of the symmetry of 9C data, the triplication is now seen in the XZ-component (Figure 10), instead in the YZ-component (Figure 9). The position of the qP-wave cross talks into the ZX-component (Figure 10), rather than the YZ-component (Figure 9). The dominant qP still remains in the ZZ-component (Figure 10).

In comparing field and synthetic traces (Figures 9 and 10), it should be remembered that the inversion solution fits only slowness and polarization vectors at the 3C geophones. Absolute amplitudes, wavelet shapes, and total traveltimes are not fitted. This has two consequences: first, the properties of the overburden are not constrained, and second, detailed comparison of the observed and predicted traces has no direct correspondence with the overburden structure. The observed and predicted traces would match only if the overburden is a single homogeneous layer with the same properties as those at the geophone, or if variations in the overburden are independently determined and so can be incorporated into the modeling. In the present context, the overburden is relatively homogeneous (Figure 2), hence, the fairly good fit between the predicted and observed traveltimes (Figures 9 and 10). To determine the properties of each layer in a heterogeneous section requires recording with 3C geophones in each layer.

DISCUSSION

For the field data, all the polarization measurements and the vertical phase slownesses are independent of the complexity of the overburden as they are local to the downhole receivers (e.g., Dewangan and Grechka, 2003; Nistala and McMechan, 2005). The vertical phase slowness local to the receiver is the derivative of the traveltime in the vertical direction. The vertical slownesses are calculated for all source azimuths and offsets to sample a wide range of slownesses.

The horizontal slownesses cannot be measured in a vertical hole, but may be approximated by differencing times between pairs of sources at the surface for a receiver at a fixed depth in the borehole. Horizontal slowness is approximated by the averaged slowness near each source at the surface. Structural complexity in the overburden may influence the accuracy of the horizontal phase slowness estimates made at the surface (e.g., Gaiser, 1990; Sayers, 1997). Alternatively, the horizontal slownesses may be estimated along with the elastic tensor elements, rather than being input. Both approaches are used above and both give similar results for the present data set.

The overburden structure of the Weyburn Field is relatively simple (Figure 2); there is a regional dip of 0.5° (Adam, 2003) and the most lateral velocity variation is 1.5% (Jenner, 2001), so lateral heterogeneity will not significantly influence the inversion results. There is only a small amount of vertical heterogeneity in lithology above the recording depth (Figure 2), so its effect on the range of available incident angles, via angle deviation by refraction, is minimal. If this is sufficiently strong, the solution without horizontal slownesses in the input will be preferable. For the present data, the two solutions with and without the horizontal slownesses are essentially identical (Figure 6 and tensors A-2 and A-3 in Appendix A), indicating that the approximation of a homogeneous overburden is acceptable for this data set; if it were not, the two solutions would be different.

The computation times for the two solutions are different because the sizes of the respective problems are different. The nine iterations to solve for the 21 data moduli (Figure 6a and 6b) took about three minutes on a single model 6600 Intel(R) Core (TM)2 with a 2.40 GHz clock (for the phase slownesses and polarizations of qP, qS₁, and qS₂ from 1253 3C sources at one 3C borehole receiver). The eleven iterations to solve for the 21 elastic moduli and the 7518 horizontal slowness components (1253 sources \times 3 wave types \times 2 horizontal slowness components) (Figure 6d and 6e) took ~ 45 minutes on the same machine.

The 9C wide azimuth data provide advantages compared with 3C data to estimate elastic tensor elements because the qP, qS₁, and qS₂ events are well captured, identified, and fitted. An important aspect of the present data set is that the slowness and polarization apertures are sufficiently wide that the elastic tensor is well sampled (see Rusmanugroho and McMechan, 2012). The 3C sources provide better data than 1C sources; for example, shear waves produced by horizontal sources are higher quality and amplitude than those produced by a vertical source (Hardage et al., 2003).

The inversion and forward modeling indicate that the anisotropic symmetry of the Weyburn Field is orthorhombic, dominated by a very strong VTI, with minor but detectable, near vertical fractures. Some authors (e.g., Jones and Wang, 1981; Adam, 2003) conclude that the Williston basin or Weyburn Field possess VTI anisotropy. However, Bunge (2001) also notes that there are some fracture sets identified in the borehole cores and logs between 50° and 65° azimuth relative to the inline direction, which is consistent with our estimate of $\sim 55^\circ$. Thus, the core data support the VSP inversion results.

In future research, the elastic moduli may be interpreted using the reverse process of the forward modeling of the effective medium theory (e.g., Jakobsen et al., 2003) to estimate the rock and crack properties such as crack density, crack orientation, and fluid content for characterization of fractured reservoirs. This is also an inversion problem.

CONCLUSIONS

The Christoffel-equation-based inversion for 21 elastic tensor elements has produced an acceptable solution as indicated by the similarities in the observed slowness and polarization data, and in those data synthesized from the inverted tensor. A final forward modeling provides an independent check on the solution; the simulated synthetic seismograms are close to the field data. Inversion and forward modeling indicate that the anisotropic symmetry of the Weyburn Field is orthorhombic, dominantly VTI, with minor near-vertical fractures oriented about 55° to the inline direction. The orthorhombic symmetry is inferred from the number and relative values of the nonzero elements of the inverted elastic tensor. The processing illustrates a viable workflow for estimating and evaluating elastic moduli from 9C VSP data.

ACKNOWLEDGMENTS

The research leading to this paper was supported by the Sponsors of the UT-Dallas Geophysical Consortium. We would like to thank the Reservoir Characterization Project at the Colorado School of Mines and the Geological Survey of Canada (GSC) for providing the field VSP data. Special thanks to Gilles Bellefleur of the GSC for providing information about the data preprocessing. Constructive reviews by the reviewers are much appreciated. Figure 2 is

included via the “fair use” provision of GSA Today. This paper is Contribution No. 1231 from the Geosciences Department at the University of Texas at Dallas.

APPENDIX A

THE ELASTIC MODULI

The starting model is homogeneous and isotropic. The isotropic, density-normalized elastic tensor \mathbf{c} (km^2/s^2) calculated using the host rock parameters from Jones and Wang (1981) (P-wave velocity (V_p) 3250 m/s, S-wave velocity (V_s) 1625 m/s, and bulk density (ρ) 2240 kg/m^3) is

$$\mathbf{c} = \begin{pmatrix} 10.5625 & 5.2813 & 5.2813 & 0 & 0 & 0 \\ 5.2813 & 10.5625 & 5.2813 & 0 & 0 & 0 \\ 5.2813 & 5.2813 & 10.5625 & 0 & 0 & 0 \\ 0 & 0 & 0 & 2.6406 & 0 & 0 \\ 0 & 0 & 0 & 0 & 2.6406 & 0 \\ 0 & 0 & 0 & 0 & 0 & 2.6406 \end{pmatrix}. \quad (\text{A-1})$$

Inversion for the density-normalized 21 component elastic tensor \mathbf{c} (km^2/s^2) with approximated horizontal slownesses included in the input, converged in seven iterations (Figure 6b). The result is

$$\mathbf{c} = \begin{pmatrix} 6.6167 & 3.2338 & 3.6013 & 0.0017 & -0.0020 & 0.0133 \\ 3.2338 & 6.5975 & 3.5951 & 0.0027 & -0.0011 & 0.0126 \\ 3.6013 & 3.5951 & 4.6660 & 0.0030 & -0.0020 & 0.0086 \\ 0.0017 & 0.0027 & 0.0030 & 0.5320 & 0.0026 & -0.0002 \\ -0.0020 & -0.0011 & -0.0020 & 0.0026 & 0.5339 & 0.0004 \\ 0.0133 & 0.0126 & 0.0086 & -0.0002 & 0.0004 & 1.6874 \end{pmatrix}. \quad (\text{A-2})$$

Inversion for the density-normalized 21 component elastic tensor \mathbf{c} (km^2/s^2) without horizontal slownesses in the input, converged in nine iterations (Figure 6e). The result is

$$\mathbf{c} = \begin{pmatrix} 6.6050 & 3.2178 & 3.5930 & 0.0011 & -0.0019 & 0.0123 \\ 3.2178 & 6.5731 & 3.5811 & 0.0026 & -0.0019 & 0.0129 \\ 3.5930 & 3.5811 & 4.6589 & 0.0030 & -0.0028 & 0.0080 \\ 0.0011 & 0.0026 & 0.0030 & 0.5322 & 0.0032 & 0.0000 \\ -0.0019 & -0.0019 & -0.0028 & 0.0032 & 0.5334 & 0.0001 \\ 0.0123 & 0.0129 & 0.0080 & 0.0000 & 0.0001 & 1.6883 \end{pmatrix}. \quad (\text{A-3})$$

REFERENCES

- Adam, L., 2003, Anisotropic parameter estimation from borehole data at Weyburn Field: Uncertainty and resolution: M.S. thesis, Colorado School of Mines.
- Alford, R. M., 1986, Shear data in the presence of azimuthal anisotropy: Dilley, Texas: 5th Annual International Meeting, SEG, Expanded Abstracts, 476–479.
- Bellefleur, G., L. Adam, D. White, B. Mattocks, and T. Davis, 2003, Seismic imaging and anisotropy analysis of 9C 3D-VSP data at Weyburn Field, Saskatchewan, Canada: 73rd Annual International Meeting, SEG, Expanded Abstracts, 1326–1329.
- Bellefleur, G., D. White, and T. Davis, 2004, P-wave imaging using 3D-VSP data in VTI media, Weyburn Field, Saskatchewan Canada: 74th Annual International Meeting, SEG, Expanded Abstracts, 2521–2524.
- Bunge, R. J., 2001, Midale reservoir fracture characterization using integrated well and seismic data, Weyburn Field, Saskatchewan: M.S. thesis, Colorado School of Mines.
- Carcione, J. M., 2007, Wave fields in real media: Elsevier.
- Cerjan, C., D. Kosloff, R. Kosloff, and M. Reshef, 1985, A nonreflecting boundary condition for discrete acoustic and elastic wave equations: *Geophysics*, **50**, 705–708, doi: [10.1190/1.1441945](https://doi.org/10.1190/1.1441945).
- Crampin, S., 1991, Effects of point singularities on shear-wave propagation in sedimentary basins: *Geophysical Journal International*, **107**, 531–543, doi: [10.1111/gji.1991.107.issue-3](https://doi.org/10.1111/gji.1991.107.issue-3).
- Davis, T. L., M. J. Terrel, R. D. Benson, and R. R. Kendall, 2002, Seismic monitoring of the CO₂ flood at Weyburn Field, Saskatchewan, Canada: 64th Annual International Conference and Exhibition, EAGE, Extended Abstracts, Z99.
- Dellinger, J. A., 1991, Anisotropic seismic wave propagation: Ph.D. thesis, Stanford University.
- de Parscau, J., and L. Nicoletis, 1990, Transverse isotropy estimation from multioffset VSPs: 60th Annual International Meeting, SEG, Expanded Abstracts, 1439–1442.
- Dewangan, P., and V. Grechka, 2003, Inversion of multicomponent, multi-azimuth, walkaway VSP data for the stiffness tensor: *Geophysics*, **68**, 1022–1031, doi: [10.1190/1.1581073](https://doi.org/10.1190/1.1581073).
- DiSiena, J. P., J. E. Gaiser, and D. Corrigan, 1984, Horizontal components and shear wave analysis of three-component VSP data, in M. N. Toksöz, and R. R. Steward, eds., Vertical seismic profiling, Part B: Advanced concepts: Geophysical Press, 177–188.
- Ditri, J. J., 1994, On determination of the elastic moduli of anisotropic media from limited acoustic data: *Journal of the Acoustical Society of America*, **95**, 1761–1767, doi: [10.1121/1.408695](https://doi.org/10.1121/1.408695).
- Gaiser, J. E., 1990, Transversely isotropic phase velocity analysis from slowness estimates: *Journal of Geophysical Research*, **95**, 11241–11254, doi: [10.1029/JB095iB07p11241](https://doi.org/10.1029/JB095iB07p11241).
- Hardage, B. A., M. DeAngelo, and P. Murray, 2003, Defining P-wave and S-wave stratal surfaces with nine-component VSPs: *The Leading Edge*, **22**, 720–729, doi: [10.1190/1.1605072](https://doi.org/10.1190/1.1605072).
- Helbig, K., 1994, Foundations of anisotropy for exploration seismics: Pergamon.
- Jakobsen, M., J. A. Hudson, and T. A. Johansen, 2003, T-matrix approach to shale acoustics: *Geophysical Journal International*, **154**, 533–558, doi: [10.1046/j.1365-246X.2003.01977.x](https://doi.org/10.1046/j.1365-246X.2003.01977.x).
- Jech, J., 1991, Computation of elastic parameters of anisotropic medium from travel times of quasi-compressional waves: *Physics of the Earth and Planetary Interiors*, **66**, 153–159, doi: [10.1016/0031-9201\(91\)90074-R](https://doi.org/10.1016/0031-9201(91)90074-R).
- Jenner, E., 2001, Azimuthal anisotropy of 3-D compressional wave seismic data, Weyburn Field, Saskatchewan: M.S. thesis, Colorado School of Mines.
- Jones, L. E. A., and H. F. Wang, 1981, Ultrasonic velocities in Cretaceous shales from the Williston basin: *Geophysics*, **46**, 288–297, doi: [10.1190/1.1441199](https://doi.org/10.1190/1.1441199).
- Kochetov, M., and M. A. Slawinski, 2009, Estimating effective elasticity tensors from Christoffel equations: *Geophysics*, **74**, no. 5, WB67–WB73, doi: [10.1190/1.3155163](https://doi.org/10.1190/1.3155163).
- Menke, W., 1989, Geophysical data analysis: Discrete inverse theory: Academic Press.
- Michaud, G., 2001, Time-lapse multicomponent borehole seismic monitoring of a pilot CO₂ flood: Ph.D. thesis, Colorado School of Mines.
- Moré, J. J., 1977, The Levenberg-Marquardt algorithm: Implementation and theory, in G. A. Watson, ed., Numerical analysis: Lecture notes in mathematics: Springer Verlag, **630**, 105–116.
- Nistala, S., and G. A. McMechan, 2005, 3D modeling of fracture-induced shear-wave splitting in the southern California basin: *Bulletin of the Seismological Society of America*, **95**, 1090–1100, doi: [10.1785/0120040225](https://doi.org/10.1785/0120040225).
- Norris, A. N., 1989, On the acoustic determination of the elastic moduli of anisotropic solids and acoustic conditions for the existence of symmetry planes: *Journal of Mechanics and Applied Mathematics*, **42**, no. S1, 413–426, doi: [10.1121/1.2026810](https://doi.org/10.1121/1.2026810).
- Ramos-Martínez, J., A. A. Ortega, and G. A. McMechan, 2000, 3-D seismic modeling for cracked media: Shear-wave splitting at zero-offset: *Geophysics*, **65**, 211–221, doi: [10.1190/1.1444712](https://doi.org/10.1190/1.1444712).
- Reasnor, M. D., 2001, Forward modeling and interpretation of multicomponent seismic data for fracture characterization, Weyburn Field, Saskatchewan: M.S. thesis, Colorado School of Mines.
- Rusmanugroho, H., and G. A. McMechan, 2010, Modeling sensitivity of 3D, 9-C wide azimuth data to changes in fluid content and crack density in cracked reservoirs: *Geophysics*, **75**, no. 5, T155–T165, doi: [10.1190/1.3479555](https://doi.org/10.1190/1.3479555).
- Rusmanugroho, H., and G. A. McMechan, 2012, Sensitivity of estimated elastic moduli to completeness of wave type, measurement type, and illumination apertures at a receiver in multicomponent VSP data: *Geophysics*, **77**, no. 1, R1–R18, doi: [10.1190/geo2010-0410.1](https://doi.org/10.1190/geo2010-0410.1).
- Sayers, C. M., 1997, Determination of anisotropic velocity models from walkway VSP data acquired in the presence of dip: *Geophysics*, **62**, 723–729, doi: [10.1190/1.1444182](https://doi.org/10.1190/1.1444182).

- Sun, R., and G. A. McMechan, 2008, Amplitude effect of the free surface in elastic reverse-time extrapolation: *Geophysics*, **73**, no. 5, S177–S184, doi: [10.1190/1.2953977](https://doi.org/10.1190/1.2953977).
- Tessmer, W. J., 1995, 3-D modelling of general material anisotropy in the presence of the free surface by a Chebyshev spectral method: *Geophysical Journal International*, **121**, 557–575, doi: [10.1111/gji.1995.121.issue-2](https://doi.org/10.1111/gji.1995.121.issue-2).
- Wegelin, A., 1984, Geology and reservoir properties of the Weyburn Field, southeastern Saskatchewan, in J. A. Lorsong, and M. A. Wilson, eds., *Oil and gas in Saskatchewan: Saskatchewan Geological Society Special Publication*, **7**, 71–82.
- White, D. J., G. Burrowes, T. Davis, Z. Hajnal, K. Hirsche, I. Hutcheon, E. Majer, B. Rostron, and S. Whittaker, 2004, Greenhouse gas sequestration in abandoned oil reservoirs: The international energy agency Weyburn pilot project: *GSA Today*, **14**, no. 7, 4–10. doi: [10.1130/1052-5173\(2004\)014<004:GGSIAO>2.0.CO;2](https://doi.org/10.1130/1052-5173(2004)014<004:GGSIAO>2.0.CO;2).
- M. Wilson, and M. Monea, eds., 2004, IEA GHG Weyburn CO₂ monitoring and storage project summary report 2002–2004, Petroleum Technology Research Center.
- Winterstein, D. F., 1990, Velocity anisotropy terminology for geophysicists: *Geophysics*, **55**, 1070–1088, doi: [10.1190/1.1442919](https://doi.org/10.1190/1.1442919).
- Zhang, Q., 2011, Common image gathers in the angle domain from reverse-time migration in 2D isotropic acoustic, elastic, and VTI media: Ph.D. dissertation, The University of Texas at Dallas.
- Zhang, Q., and G. A. McMechan, 2011, Common image gathers in the incident phase angle domain from reverse-time migration in 2D elastic VTI media: *Geophysics*, **76**, no. 6, S197–S206, doi: [10.1190/geo2011-0015.1](https://doi.org/10.1190/geo2011-0015.1).
- Zheng, X., and I. Pšenčík, 2002, Local determination of weak anisotropy parameters from qP-wave slowness and particle motion measurements: *Pure and Applied Geophysics*, **159**, 1881–1905, doi: [10.1007/s00024-002-8713-z](https://doi.org/10.1007/s00024-002-8713-z).